

Splashback radius of nonspherical dark matter halos from cosmic density and velocity fields

Teppei Okumura,^{1,2,*} Takahiro Nishimichi,^{2,3} Keiichi Umetsu,¹ and Ken Osato⁴

¹*Institute of Astronomy and Astrophysics, Academia Sinica, P. O. Box 23-141, Taipei 10617, Taiwan*

²*Kavli Institute for the Physics and Mathematics of the Universe (WPI),*

UTIAS, The University of Tokyo, Kashiwa, Chiba 277-8583, Japan

³*CREST, JST, 4-1-8 Honcho, Kawaguchi, Saitama, 332-0012, Japan*

⁴*Department of Physics, University of Tokyo, 7-3-1 Hongo, Bunkyo-ku, Tokyo 113-0033 Japan*

(Dated: July 23, 2018)

We investigate the splashback features of dark-matter halos based on cosmic density and velocity fields. Besides the density correlation function binned by the halo orientation angle, which was used in the literature, we introduce, for the first time, the corresponding velocity statistic, alignment momentum correlation function, to take into account the asphericity of halos. Using large-volume, high-resolution N -body simulations, we measure the alignment statistics of density and velocity. On halo scales, $x \sim R_{200m} \sim 1 h^{-1}$ Mpc, we detect a sharp steepening in the momentum correlation associated with the physical halo boundary, or the splashback feature, which is found more prominent than in the density correlation. We also find that the splashback radius determined from the density correlation becomes $\sim 3.5\%$ smaller than that from the momentum correlation, with their correlation coefficient being 0.605. Moreover, the orientation-dependent splashback feature due to halo asphericity is measured when the density profile is determined by dark-matter particles, which can be used as a test of collisional cold dark matter since the halo shape is predicted to be rounder in such a model.

I. INTRODUCTION

In the current paradigm of cosmic structure formation, galaxies, which are observed as a tracer of the large-scale structure of the Universe, are considered to be formed within dark-matter halos. Besides, modeling a halo power spectrum is the important first step to properly interpreting the observed galaxy clustering, from which to extract cosmological information. Dark-matter halos thus play a fundamental role in both structure formation and cosmological studies (e.g., Refs. [1, 2]).

Recently, the phase-space structure in halo outskirts has been extensively studied based on N -body simulations, leading to the discovery of a steepening in the outer density profile of dark-matter halos [3]. This feature is interpreted as a sharp density enhancement associated with the orbital apocenter of the recently accreted matter in the growing halo potential. The location of this steepening is referred to as the splashback radius, R_{sp} , and depends on cosmology as well as on halo mass and redshift. The splashback radius provides a physical boundary of halos [3–6], and is related to the transition scale between the one-halo and two-halo regimes in the galaxy power spectrum or correlation function to a certain extent [1, 5].

Using efficient cluster-finding algorithms based on the observed galaxy distribution [7, 8], the splashback features have been studied by observing the galaxy density profile and weak lensing profile [9–12] (see Ref. [13] for difficulties in observing the splashback feature). Further studies revealed that dynamical friction acting on

massive subhalos orbiting in their parent clusters makes splashback features appear at smaller cluster radii [14–16]. However, the detected splashback radius is found to be significantly smaller than predicted by N -body simulations, even though the effect of dynamical friction is considered [9, 12]. Thus, careful work is required both from theoretical and observational aspects.

Splashback features are determined by the orbits of dark matter around halo centers and thus fully characterized in phase space. Hence, the commonly used density statistic alone cannot capture the full dynamical information. Furthermore, the two-halo term of the density statistic is enhanced by the galaxy bias, whereas its impact on the determination of the splashback radius has not been discussed in the literature. Another important fact on precisely measuring the splashback radius is that halos are aspherical. Thus, spherical averaging would smear out the splashback features [17]. While the caustic techniques have been extensively studied in phase space to measure dynamical mass profiles of clusters from infall velocity patterns [18–22], these analyses have not been performed in the context of splashback studies. In this paper, we present a detailed study of splashback features based on both density and velocity statistics, focusing on the issues described above.

This paper is organized as follows. In Sec. II, we present the formalism of alignment density and velocity statistics used to study the splashback features. Section III describes the N -body simulations and how we construct mock cluster and galaxy samples. Section IV presents measurements of alignment density and momentum correlation functions, their splashback features, and constraints on the splashback radius. Our conclusions are given in Sec. V.

*Electronic address: tokumura@asiaa.sinica.edu.tw

II. FORMALISM

The three-dimensional density profile around clusters is computed by the cross-correlation functions between halo centers and mass tracers. When dark matter particles and galaxies are used as the tracers, the cross-correlations are, respectively, expressed as $\xi_{mc}(r) = \langle \delta_m(\mathbf{x}_1) \delta_c(\mathbf{x}_2) \rangle$ and $\xi_{gc}(r) = \langle \delta_g(\mathbf{x}_1) \delta_c(\mathbf{x}_2) \rangle$ (e.g., see Ref. [23]), where $r = |\mathbf{r}| = |\mathbf{x}_2 - \mathbf{x}_1|$ and δ_c , δ_g , and δ_m are the overdensity fields traced by clusters, galaxies, and matter, respectively. In weak lensing and galaxy redshift surveys, one can, respectively, observe the weak lensing profile, $\Sigma(R)$ [or $\Delta\Sigma(R)$], and the galaxy density profile, $\Sigma_g(R)$, which are the line-of-sight projection of the cross-correlation functions, $\xi_{mc}(\mathbf{r})$ and $\xi_{gc}(\mathbf{r})$.

A. Alignment density correlation

To take into account the asphericity of dark matter halos, we consider the angle-binned or alignment correlation function [24–26], an extension of the conventional matter and galaxy density profiles around clusters, respectively, $\xi_{mc}(r)$ and $\xi_{gc}(r)$, by taking account of the orientations of the clusters,

$$\xi_{Ac}(r, \theta) = \langle \delta_A(\mathbf{x}_1, \theta) \delta_c(\mathbf{x}_2) \rangle, \quad (1)$$

where $A = \{m, g\}$. Here, θ is the angle between the elongated orientation of cluster halos, defined by the major axis of ellipsoidal halo shapes, and the separation vector \mathbf{r} . The conventional correlation function can be obtained by integrating over θ ,

$$\xi_{Ac}(r) = \int_0^1 d \cos \theta \xi_{Ac}(r, \theta). \quad (2)$$

The alignment correlation is related to the density-ellipticity correlation, a main source of contamination for measurements of the gravitational shear power spectrum in weak lensing surveys, also known as intrinsic alignments, $\xi_{g+}(\mathbf{r}) = \langle \delta_g(\mathbf{x}_1) [1 + \delta_c(\mathbf{x}_2)] \gamma^I(\mathbf{x}_2) \rangle$, where $\gamma^I(\mathbf{x}) = \frac{1-q^2}{1+q^2} \cos(2\theta_p)$, θ_p is the angle projected onto the celestial sphere, and q is the minor-to-major-axis ratio of halos [27–34]. This function is related to the alignment correlation function by

$$\tilde{\xi}_{g+}(\mathbf{r}) = (2/\pi) \int_0^{\pi/2} d\theta \cos(2\theta_p) \xi_{gc}(\mathbf{r}, \theta_p), \quad (3)$$

where $\tilde{\xi}_{g+}$ is the same as ξ_{g+} but with q fixed to $q = 0$ [25, 35, 36]. While these two statistics are complimentary to each other, we will focus on the alignment correlation function because it provides direct insight on how the matter is distributed along and perpendicular to the major axis of halos.

B. Alignment velocity statistics

Next we consider a statistic with respect to the cosmic velocity field, the momentum correlation function [37–41], $\psi_{Ac}(r) = \langle [1 + \delta_A(\mathbf{x}_1)] [1 + \delta_c(\mathbf{x}_2)] \mathbf{v}_A(\mathbf{x}_1) \cdot \mathbf{v}_c(\mathbf{x}_2) \rangle$, where \mathbf{v}_A is the peculiar velocity of field A (namely, the cosmic expansion term is not included) [63]. We propose using this momentum correlation as a probe of the splashback radius because the splashback features are fully characterized in phase space. In analogy to the density statistic, we define the alignment momentum correlation, $\psi_{Ac}(r, \theta)$, by replacing $\delta_A(\mathbf{x}_1)$ in the above equation by $\delta_A(\mathbf{x}_1, \theta)$,

$$\psi_{Ac}(r, \theta) = \langle [1 + \delta_A(\mathbf{x}_1, \theta)] [1 + \delta_c(\mathbf{x}_2)] \times \mathbf{v}_A(\mathbf{x}_1) \cdot \mathbf{v}_c(\mathbf{x}_2) \rangle. \quad (4)$$

This and Eq. (1) are the main statistics we use to investigate the splashback features of nonspherical dark halos. Similarly to the density case, the conventional momentum correlation, $\psi_{Ac}(\mathbf{r})$, can be obtained by averaging Eq. (4) over θ ,

$$\psi_{Ac}(r) = \int_0^1 d \cos \theta \psi_{Ac}(r, \theta). \quad (5)$$

We also introduce the angle-binned, density-weighted pairwise velocity dispersion:

$$\sigma_{v,Ac}^2(r, \theta) = \langle [1 + \delta_A(\mathbf{x}_1, \theta)] [1 + \delta_c(\mathbf{x}_2)] \times |\mathbf{v}_A(\mathbf{x}_1) - \mathbf{v}_c(\mathbf{x}_2)|^2 \rangle. \quad (6)$$

However, its behavior is found to be essentially similar to that of ψ_{Ac} , and hence we do not present this statistic in this paper. Moreover, we define the angle-binned pairwise infall momentum, $p_{Ac}(r, \theta) = \langle [1 + \delta_A(\mathbf{x}_1, \theta)] [1 + \delta_c(\mathbf{x}_2)] [\mathbf{v}_A(\mathbf{x}_1) - \mathbf{v}_c(\mathbf{x}_2)] \cdot \hat{\mathbf{r}} \rangle$, where the hat denotes a unit vector. Since the splashback feature is smeared out in this statistic by construction, we do not show it in this paper [64].

III. N-BODY SIMULATIONS

To study splashback features, we use a series of large and high-resolution N -body simulations of the Λ CDM cosmology seeded with Gaussian initial conditions. These are performed as a part of the **dark emulator** project [42]. We adopt the cosmological parameters of $\Omega_m = 1 - \Omega_\Lambda = 0.315$, $\Omega_b = 0.0492$, $h = 0.673$, $n_s = 0.965$, and $\sigma_8 = 0.8309$. We employ $n_p = 2048^3$ particles of mass $m_p = 1.02 \times 10^{10} M_\odot / h$ in a cubic box of side $L_{\text{box}} = 1 h^{-1} \text{ Gpc}$. We use 24 realizations in total and analyze the snapshots at $z = 0.306$.

Subhalos are identified using the ROCKSTAR algorithm [43] from phase-space information of matter particles. The velocity of each subhalo is determined by the average particle velocity within the innermost 10% of the

TABLE I: Properties of mock central/satellite subhalo samples at $z = 0.306$. f_{sat} is the number fraction of satellites, M_{min} and \bar{M} are the minimum and average masses of central subhalos in units of $10^{12}h^{-1}M_{\odot}$, respectively; \bar{n} is the number density in units of $h^3\text{Mpc}^{-3}$; and b_A ($A = \{c, g\}$) is the cluster/galaxy bias computed at the large-scale limit.

Halo types	Label	f_{sat}	M_{min}	\bar{n}	b_A	\bar{M}
Clusters (central)	c	0	100	2.05×10^{-5}	3.05	188
Galaxies (central + satellite)	g	0.137	0.224	5.58×10^{-4}	1.69	27.9

subhalo radius. We use the standard definition for the halo radius and mass,

$$M_h \equiv M_{\Delta m} = M(< R_{\Delta m}) = (4\pi/3)\Delta\rho_m(z)R_{\Delta m}^3, \quad (7)$$

where ρ_m is the mean mass density of the Universe at given redshift z , and we adopt $\Delta = 200$. In the ROCKSTAR algorithm, if one subhalo is within the virial radius of another subhalo but the opposite is not the case, the latter halo is labeled as a central subhalo. On the other hand, if two or more subhalos are located within the virial radius of each other, the most massive one is labeled as a central subhalo, and another is labeled as (a) satellite subhalo(s).

To study cluster-scale halos, we select central subhalos with $M_h \geq 10^{14}h^{-1}M_{\odot}$, which roughly corresponds to the typical threshold of the richness parameters used by the cluster-finding algorithms in the literature. We create mock galaxy catalogs using a halo occupation distribution (HOD) model [44] applied for the LOWZ galaxy sample of the SDSS-III Baryon Oscillation Spectroscopic Survey obtained by Ref. [45]. We populate halos with galaxies according to the best-fitting HOD $N(M_h)$. For halos that contain satellite galaxies, we randomly draw $N(M_h) - 1$ member satellite subhalos to mimic the positions and velocities of the satellites (see Refs. [46, 47] for alternative methods). We use a random selection of subhalos rather than the largest subhalos, because a satellite subhalo undergoes the effect of a tidal disruption in the host halo and its mass decreases as it goes toward the center of the gravitational potential. Thus, if we selected the largest satellite subhalos to host galaxies, we would preferentially pick up the satellite subhalos residing at the outskirts of the gravitational potential, which conflicts with the galaxy distribution in observation. For this HOD prescription we use all the subhalos with 20 or more than particles in the simulation box. We assume central subhalos to have triaxial shapes and estimate the orientations of their major axes using the second moments of the mass distribution [48]. Table I summarizes properties of our mock samples.

IV. NUMERICAL ANALYSIS

A. Measurements

Since one usually considers a correlation function projected along the line of sight in observational studies, the splashback features are smeared out to some extent by projection effects. On the other hand, since we are interested in physical properties of the splashback radius, we present the alignment density and velocity correlation statistics in three-dimensional (3D) space. The alignment correlation function of the galaxy density and cluster shape can be measured by

$$\xi_{gc}(r, \theta) = \frac{\langle D_g D_c \rangle}{\langle R_g R_c \rangle} - 1, \quad (8)$$

where $\langle D_g D_c \rangle(r, \theta)$ and $\langle R_g R_c \rangle(r, \theta)$ are, respectively, the normalized pair counts of the data and their randoms as functions of separation, r , and position angle of clusters, θ . Note that $\langle R_g R_c \rangle$ can be analytically computed since we place the periodic boundary condition on the simulation box. The momentum correlation function can be measured by

$$\psi_{gc}(r, \theta) = \frac{\langle \mathbf{V}_g \cdot \mathbf{V}_c \rangle}{\langle R_g R_c \rangle}, \quad (9)$$

where $\langle \mathbf{V}_g \cdot \mathbf{V}_c \rangle(r, \theta)$ is the normalized pair count of galaxies and clusters weighted by the scalar product of their velocities as functions of r and θ . We also compute the same statistics, but galaxies are replaced by dark matter as a density/velocity tracer, namely, $\xi_{mc}(r, \theta)$ and $\psi_{mc}(r, \theta)$. In the following analysis, we measure these statistics from each of the 24 realizations and present their means. We also compute the standard errors from the scatters, but we do not show them since the errors are negligibly small.

The top-left panel of Fig. 1 shows the cluster-galaxy cross-correlation function binned in the cluster angle θ for the density field and that for the velocity field. The top-right panel is the same as the top-left panel but shows the cluster-dark matter cross-correlation function. The bottom panels present the ratios of the alignment statistic to the conventional one, $X_{gc}(r, \theta)/X_{gc}(r)$ and $X_{mc}(r, \theta)/X_{mc}(r)$, where $X = \{\xi, \psi\}$. The deviation from unity is the evidence of halo-shape alignments.

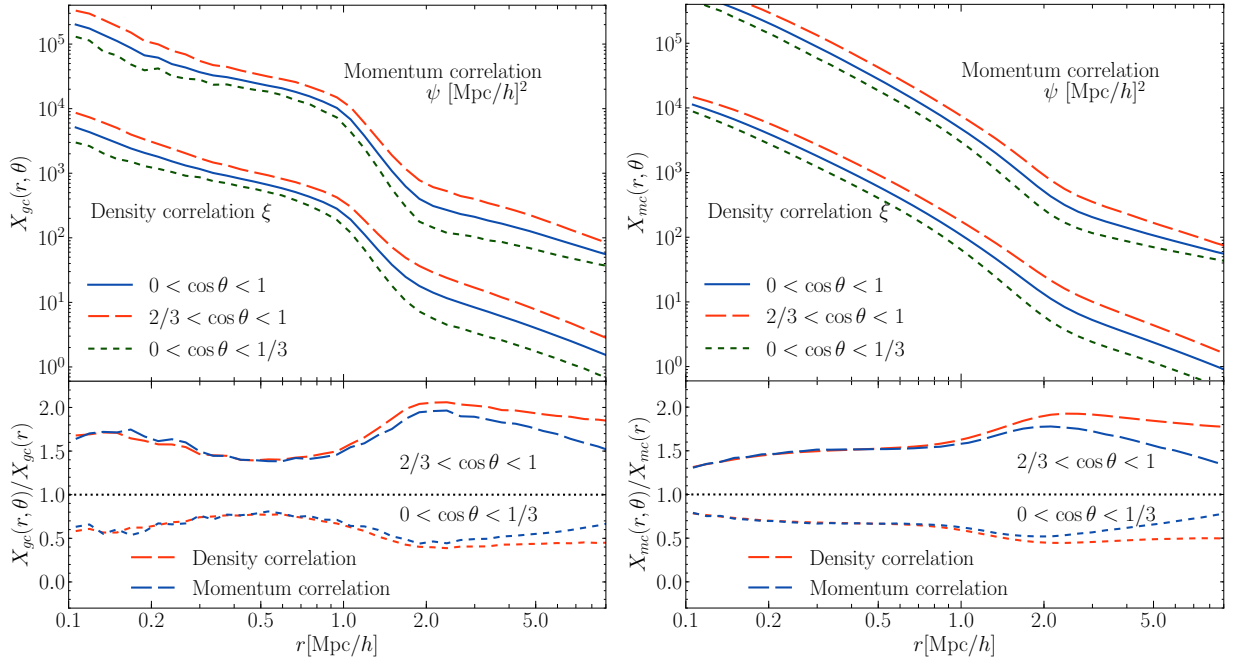


FIG. 1: Top left: Alignment density correlation (lower lines) and momentum correlation (upper lines) of galaxies and clusters. The dashed and dotted lines respectively show the correlations parallel and perpendicular to the major axes of the clusters, $X_{gc}(r, \theta)$, while the solid lines are the conventional, angle-averaged statistics, $X_{gc}(r)$, where $X = \{\xi, \psi\}$. Bottom left: Ratios of angle-binned correlations to the conventional ones between galaxies and clusters, $X_{gc}(r, \theta)/X_{gc}(r)$. Top right: Same as the top-left panel but the alignment correlation functions of dark matter and clusters, $X_{mc}(r, \theta)$. Bottom right: Ratios of angle-binned correlations to the conventional ones between dark matter and clusters, $X_{mc}(r, \theta)/X_{mc}(r)$.

While this effect in the density correlation has been extensively studied both theoretically and observationally [25, 49–51], that in the momentum correlation is measured by us for the first time.

Using the cluster-galaxy and cluster-dark matter cross-correlation functions, one can determine the galaxy density and momentum biases, respectively, as

$$b_g(r) = \frac{\xi_{gc}(r)}{\xi_{mc}(r)}, \quad b_p(r) = \frac{\psi_{gc}(r)}{\psi_{mc}(r)}. \quad (10)$$

On sufficiently large scales in which linear perturbation theory is believed to be applicable, they approach constants, and particularly we have $b_p = 1$ in the absence of the velocity bias. See Ref. [52] for redshift and halo mass dependences of these bias parameters. We present the density bias and momentum bias in the left and right panels of Fig. 2, respectively. The horizontal blue lines are the bias values at the large-scale limit. As studied in detail by Ref. [52], the density bias approaches the linear bias on smaller scales than the momentum bias.

B. Splashback features

On the scale of $x \sim 1 h^{-1} \text{Mpc}$, an abrupt change in the slope of both the density and momentum correlations can be seen, coinciding with the transition scale

between one-halo and two-halo regimes [1, 53]. As described in Sec. I, this steepest-slope location is regarded as a signature of the splashback radius R_{sp} [3–5, 15] if the logarithmic slope there, $\gamma = d \log \xi_{gc} / d \log r$, is steeper than the Navarro-Frenk-White (NFW) profile [54] (See

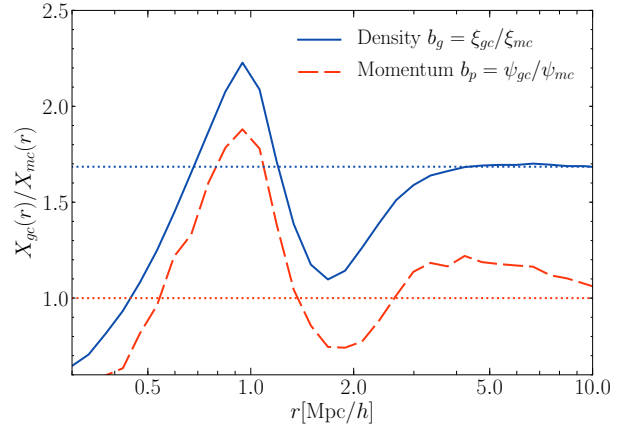


FIG. 2: Galaxy bias (blue) and momentum bias (red) obtained from the cross-correlation functions, $b_g(r) = \xi_{gc}(r)/\xi_{mc}(r)$ and $b_p(r) = \psi_{gc}(r)/\psi_{mc}(r)$, respectively. The blue and red horizontal lines represent the large-scale limit of the galaxy and momentum bias, respectively $b_g = 1.69$ and $b_p = 1$.

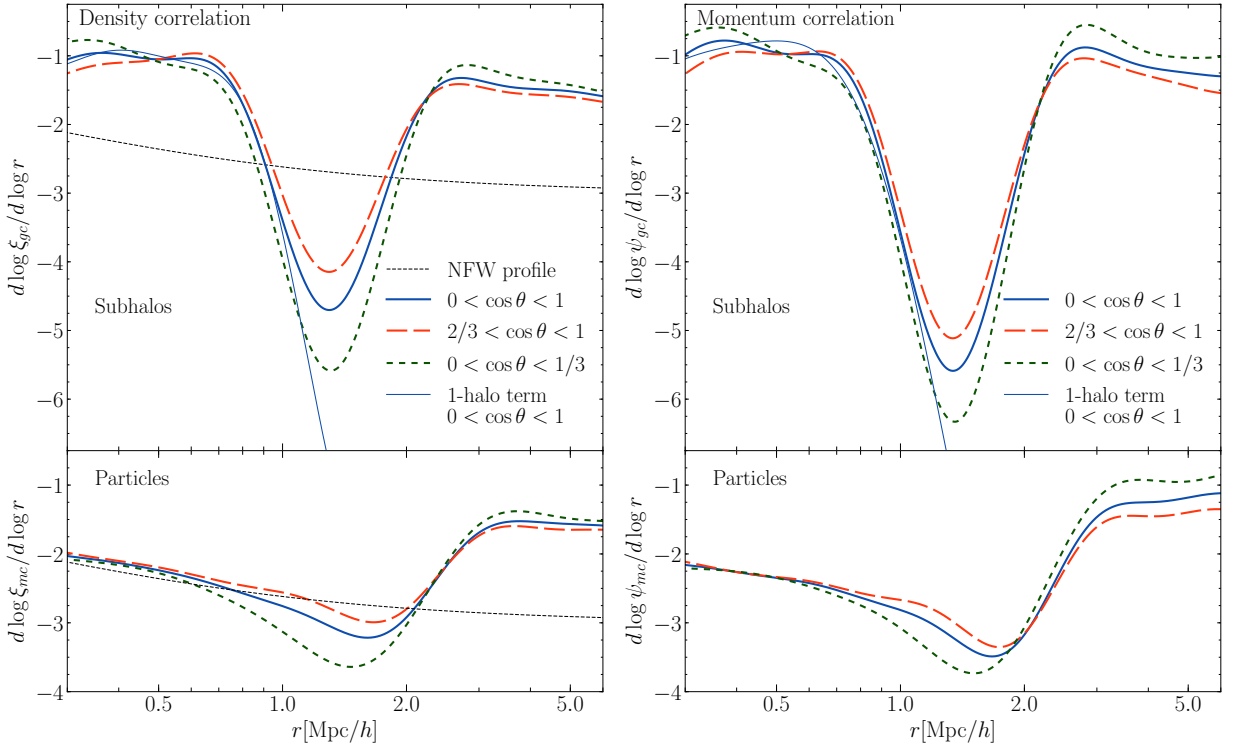


FIG. 3: Top: Logarithmic slope of the angle-binned galaxy-cluster cross-correlation of density (left) and momentum (right). The meaning of the line types and colors is the same as the top panel of Fig. 1. The thin blue solid curve is the result of the one-halo term, $d \log X_{gc}^{1h} / d \log r$. Bottom: Same as the top panels, but the density and velocity fields of galaxies are replaced by those of dark matter. The black dotted curves in the left panels are the NFW profile.

Ref. [55] for an alternative approach to defining the boundary using the satellite distribution). The top-left panel of Fig. 3 presents γ , where the derivatives are computed by interpolating the measured ξ_{gc} with the Gaussian processes [56]. We used the “squared exponential” kernel and optimized its amplitude and length parameters to fit $\log X_{gc}$ as a function of $\log r$ in the range $0.1 h^{-1} \text{ Mpc} < x < 10 h^{-1} \text{ Mpc}$ [57]. The steepest slope of our conventional correlation function reaches $\gamma \simeq -4.5$. This is significantly steeper than the NFW profile depicted as the black dotted curve ($\gamma \rightarrow -3$) and consistent with the characteristic splashback properties in ΛCDM found by Ref. [3]. Intriguingly, the slopes are shallower and steeper, respectively, for the alignment correlation parallel and perpendicular to the major axes of the clusters. This can be interpreted by the fact that the halo size varies more significantly along the direction of the major axis (i.e., smaller θ), leading to a less prominent boundary.

Likewise, we compute the logarithmic derivative for the momentum correlation, $\gamma_p = d \log \psi_{gc} / d \log r$, in the top-right panel of Fig. 3. It is interesting to note that the slope approaches $\gamma_p \rightarrow -5.5$, steeper than the boundary slope determined by the density correlation. As discussed by Ref. [58] in the context of ΛCDM structure formation, the orbital velocity anisotropy is tightly coupled with the logarithmic density slope around halos and thus expected

to be sensitive to the location of the halo edge [3], which physically and sharply separates the multistream intra-halo region from the outer infall region (see also Ref. [59]).

Another reason for the sharper splashback feature in the momentum correlation is that it is much less biased than the density correlation. Because of the nonlinear, scale-dependent bias, the steepening splashback feature probed by the density profile is further smeared out by the shallow two-halo term (See Ref. [40] for the full bias dependence on the velocity statistics). To confirm this, we split the correlation of galaxies and clusters into the correlation with those inside and outside the halo, $X_{gc} = X_{gc}^{1h} + X_{gc}^{2h}$, where $X = \{\xi, \psi\}$. We measure the one-halo terms, X_{gc}^{1h} , by cross-correlating clusters and their member galaxies identified by the phase-space friends-of-friends technique in the ROCKSTAR algorithm. We then take their derivatives, $d \log X_{gc}^{1h} / d \log r$. As shown as the blue thin curves in the top panels of Fig. 3, the logarithmic slope profiles in the one-halo regime probed by the density and momentum correlations are essentially the same, and the difference is less than a few percent around the splashback radius. This confirms that the differences in the sharpness of the steepening and the location of the steepest slope come from the two-halo terms.

To further see the effect of the bias, we also com-

pute the same derivatives, but galaxies are replaced by dark matter as a density/velocity tracer, namely, $d \log X_{mc} / d \log r$ ($X = \{\xi, \psi\}$). They are shown in the lower panels of Fig. 3. As explained in Ref. [17], the splashback feature in the mass density is smeared out compared to that traced by subhalos, because of extended substructures that are abundant in the halo outskirts. However, the slope is still steeper than that of the NFW profile as depicted by the black dotted line.

C. Constraints on the splashback radius

We constrain the splashback radius, R_{sp} and R_{sp}^p , the locations of the steepest slopes in the density correlation ($d\gamma/dr|_{r=R_{\text{sp}}} = 0$) and momentum correlation ($d\gamma_p/dr|_{r=R_{\text{sp}}^p} = 0$), respectively. The covariance error matrix is estimated by the scatter among our 24 realizations. In Fig. 4, the blue point with the error bars is the constraint from the angle-averaged halo-matter cross-correlations. The blue star represents a model prediction of Ref. [16], defined as the 75th percentile of the distribution of particle apocenters, corresponding approximately to the the radius of steepest slope in simulated halos [5].

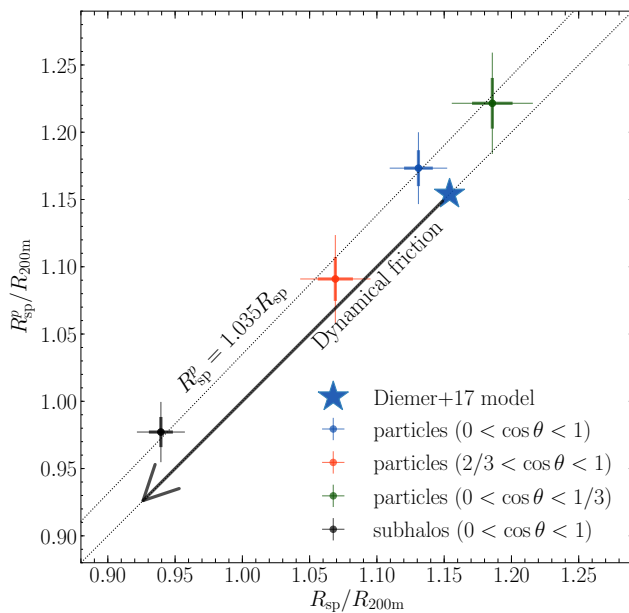


FIG. 4: Constraints on the splashback radius from the density and momentum fields, respectively shown in the horizontal and vertical axes. The blue cross is the constraints when the profile is traced by all the dark matter particles, while the green and red ones are when only the particles parallel and perpendicular to the major axis of a halo are used. The thick and thin error bars correspond to 1σ and 2σ confidence levels, respectively. The black cross is the result when the profile is traced by all the subhalos. The blue star is a prediction of Ref. [16]. The arrow indicates a range of shifts for the splashback radius due to the dynamical friction of subhalos. The upper dotted line represents $R_{\text{sp}}^p = 1.035 R_{\text{sp}}$.

For our cluster sample with $\bar{M}_{200\text{m}} = 1.88 \times 10^{14} h^{-1} M_{\odot}$, it gives $R_{\text{sp}} = 1.15 R_{200\text{m}} = 1.58 h^{-1} \text{Mpc}$, consistent with our constraints within 1σ . The green and red points are the constraints from the correlations parallel and perpendicular to the halo major axis, respectively. A clear axis dependence is detected: R_{sp} along and perpendicular to the major axis is constrained to be higher and lower than the spherically averaged value.

The resulting locations of R_{sp} and R_{sp}^p from the subhalo number density (black cross) are significantly smaller than those from matter density. This can be interpreted as the effect of dynamical friction [14]. According to Ref. [15], R_{sp} constrained from the subhalo field can be smaller than the true value by up to $\sim 20\%$ as indicated by the arrow in Fig. 4. Since we find the correlation matrix of R_{sp} and R_{sp}^p is 0.605, the momentum correlation indeed provides extra information on the splashback radius. Interestingly, the determined R_{sp} is $\sim 3.5\%$ smaller than R_{sp}^p for all the cases studied here. Hence, one can use this tight correlation to infer the value of R_{sp}^p from R_{sp} or vice versa. This slight shift is qualitatively interpreted as follows. The momentum correlation is equivalent to the density correlation weighted by velocities of tracers. As demonstrated by Ref. [5], the infall velocity reaches its (most negative) minimum at the radius larger than the splashback radius determined by the density profile. Thus, the splashback radius determined in 3D space, R_{sp} , is systematically smaller than that in phase space (six dimensions). However, this relation should be tested in more detail for different redshifts and halo masses in future work. On the other hand, the fact that the relation $R_{\text{sp}}^p = 1.035 R_{\text{sp}}$ holds for both dark matter and galaxies indicates that the galaxy bias does not affect the location of the splashback feature at the level studied in this paper.

V. CONCLUSIONS

We have proposed a velocity statistic to investigate detailed properties of the splashback radius of nonspherical dark-matter halos. The splashback radius in the momentum correlation, R_{sp}^p , has been detected for the first time from simulations. The feature is even sharper than that in the density correlation, because it separates distinct infall and multistream regions of collisionless cold dark matter. By measuring the splashback radius from both density and momentum correlations, we also demonstrated that the commonly used density statistic yields R_{sp} that is about 3.5% smaller than that expected in phase space, R_{sp}^p . In other words, the velocity field provides a less biased estimator to probe the halo boundaries. Under certain conditions, a self-interacting dark matter scenario [60] can predict a $\sim 20\%$ smaller value of the splashback radius in the satellite distribution, through the drag force acting between dark-matter particles of subhalos and cluster halos [9]. The small shift due to radial infall velocity thus needs to be taken into

account in precise theoretical modeling.

We found clear dependences of halo asphericity on splashback features: the density/velocity slopes are shallower along the halo major axis. We have also determined the orientation-dependent splashback radius using the cluster-matter density cross-correlation as well as the momentum cross-correlation. This demonstrates that the collisional feature of the cold dark matter model can be constrained by precision measurements of anisotropic splashback features because the halo shape is predicted to be rounder in such a model (see the discussion in Ref. [9]).

This paper has focused on the alignment statistics only on small, cluster scales. In a companion paper [61], we perform a comprehensive analysis by extending to larger scales, $x > 100 h^{-1} \text{ Mpc}$.

Acknowledgments

We thank Benedikt Diemer for useful comments. We also thank the anonymous referees for many useful sug-

gestions. This work was in part supported by MEXT Grant-in-Aid for Scientific Research on Innovative Areas (Grants No. 15H05887, No. 15H05893, No. 15K21733, and No. 15H05892). We acknowledge support from the Ministry of Science and Technology of Taiwan under Grants No. MOST 106-2119-M-001-031-MY3 (T. O.) and No. 103-2112-M-001-030-MY3 (K. U.). T. N. acknowledges financial support from JSPS KAKENHI Grant No. 17K14273 and JST CREST Grant No. JP-MJCR1414. K. O. is supported by Research Fellowships of JSPS for Young Scientists. K. O. acknowledges financial support from JSPS Grant-in-Aid for JSPS Research Fellow Grant No. JP16J01512. Numerical simulations were carried out on Cray XC30 at the Center for Computational Astrophysics, National Astronomical Observatory of Japan.

-
- [1] A. Cooray and R. Sheth, *Phys. Rept.* **372**, 1 (2002)
 - [2] H. Mo, F. C. van den Bosch, and S. White, *Galaxy Formation and Evolution* (2010).
 - [3] B. Diemer and A. V. Kravtsov, *Astrophys. J.* **789**, 1 (2014)
 - [4] S. Adhikari, N. Dalal, and R. T. Chamberlain, *J. Cosmol. Astropart. Phys.* **11**, 019 (2014)
 - [5] S. More, B. Diemer, and A. V. Kravtsov, *Astrophys. J.* **810**, 36 (2015)
 - [6] X. Shi, *Mon. Not. Roy. Astron. Soc.* **459**, 3711 (2016)
 - [7] E. S. Rykoff, E. Rozo, M. T. Busha, C. E. Cunha, A. Finoguenov, A. Evrard, J. Hao, B. P. Koester, A. Leauthaud, B. Nord, et al., *Astrophys. J.* **785**, 104 (2014)
 - [8] M. Oguri, *Mon. Not. Roy. Astron. Soc.* **444**, 147 (2014)
 - [9] S. More, H. Miyatake, M. Takada, B. Diemer, A. V. Kravtsov, N. K. Dalal, A. More, R. Murata, R. Mandelbaum, E. Rozo, et al., *Astrophys. J.* **825**, 39 (2016)
 - [10] K. Umetsu and B. Diemer, *Astrophys. J.* **836**, 231 (2017)
 - [11] E. Baxter, C. Chang, B. Jain, S. Adhikari, N. Dalal, A. Kravtsov, S. More, E. Rozo, E. Rykoff, and R. K. Sheth, *Astrophys. J.* **841**, 18 (2017)
 - [12] C. Chang, E. Baxter, B. Jain, C. Sánchez, S. Adhikari, T. N. Varga, Y. Fang, E. Rozo, E. S. Rykoff, A. Kravtsov, et al., *ArXiv e-prints* (2017), 1710.06808.
 - [13] P. Busch and S. D. M. White, *Mon. Not. Roy. Astron. Soc.* **470**, 4767 (2017)
 - [14] S. Adhikari, N. Dalal, and J. Clampitt, *J. Cosmol. Astropart. Phys.* **7**, 022 (2016)
 - [15] B. Diemer, *Astrophys. J. Suppl.* **231**, 5 (2017)
 - [16] B. Diemer, P. Mansfield, A. V. Kravtsov, and S. More, *Astrophys. J.* **843**, 140 (2017)
 - [17] P. Mansfield, A. V. Kravtsov, and B. Diemer, *Astrophys. J.* **841**, 34 (2017)
 - [18] J. Diemand and M. Kuhlen, *Astrophys. J. Lett.* **680**, L25 (2008)
 - [19] D. Lemze, T. Broadhurst, Y. Rephaeli, R. Barkana, and K. Umetsu, *Astrophys. J.* **701**, 1336 (2009)
 - [20] M. Vogelsberger, R. Mohayaee, and S. D. M. White, *Mon. Not. Roy. Astron. Soc.* **414**, 3044 (2011)
 - [21] K. Rines, M. J. Geller, A. Diaferio, and M. J. Kurtz, *Astrophys. J.* **767**, 15 (2013)
 - [22] J. Svensmark, R. Wojtak, and S. H. Hansen, *Mon. Not. Roy. Astron. Soc.* **448**, 1644 (2015)
 - [23] E. Hayashi and S. D. M. White, *Mon. Not. Roy. Astron. Soc.* **388**, 2 (2008)
 - [24] D. J. Paz, F. Stasyszyn, and N. D. Padilla, *Mon. Not. Roy. Astron. Soc.* **389**, 1127 (2008)
 - [25] A. Faltenbacher, C. Li, S. D. M. White, Y.-P. Jing, S. Mao, and J. Wang, *Research in Astronomy and Astrophysics* **9**, 41 (2009)
 - [26] K. Osato, T. Nishimichi, M. Oguri, M. Takada, and T. Okumura, *Mon. Not. Roy. Astron. Soc.* **477**, 2141 (2018)
 - [27] P. Catelan, M. Kamionkowski, and R. D. Blandford, *Mon. Not. Roy. Astron. Soc.* **320**, L7 (2001)
 - [28] C. M. Hirata and U. Seljak, *Phys. Rev. D* **70**, 063526 (2004)
 - [29] R. Mandelbaum, C. M. Hirata, M. Ishak, U. Seljak, and J. Brinkmann, *Mon. Not. Roy. Astron. Soc.* **367**, 611 (2006)
 - [30] T. Okumura, Y. P. Jing, and C. Li, *Astrophys. J.* **694**, 214 (2009)
 - [31] B. M. Schäfer, *International Journal of Modern Physics D* **18**, 173 (2009)
 - [32] M. A. Troxel and M. Ishak, *Phys. Rept.* **558**, 1 (2015)
 - [33] B. Joachimi, M. Cacciato, T. D. Kitching, A. Leonard, R. Mandelbaum, B. M. Schäfer, C. Sifón, H. Hoekstra, A. Kiessling, D. Kirk, et al., *Space Sci. Rev.* **193**, 1 (2015)
 - [34] E. van Uitert and B. Joachimi, *Mon. Not. Roy. Astron.*

- Soc. **468**, 4502 (2017)
- [35] T. Okumura and Y. P. Jing, *Astrophys. J. Lett.* **694**, L83 (2009)
 - [36] J. Blazek, M. McQuinn, and U. Seljak, *J. Cosmol. Astropart. Phys.* **5**, 10 (2011)
 - [37] K. Gorski, *Astrophys. J. Lett.* **332**, L7 (1988).
 - [38] K. B. Fisher, *Astrophys. J.* **448**, 494 (1995)
 - [39] M. A. Strauss and J. A. Willick, *Phys. Rept.* **261**, 271 (1995)
 - [40] T. Okumura, U. Seljak, Z. Vlah, and V. Desjacques, *J. Cosmol. Astropart. Phys.* **5**, 003 (2014)
 - [41] N. S. Sugiyama, T. Okumura, and D. N. Spergel, *J. Cosmol. Astropart. Phys.* **7**, 001 (2016)
 - [42] T. Nishimichi, et al., in preparation (2018).
 - [43] P. S. Behroozi, R. H. Wechsler, and H.-Y. Wu, *Astrophys. J.* **762**, 109 (2013)
 - [44] Z. Zheng, A. A. Berlind, D. H. Weinberg, A. J. Benson, C. M. Baugh, S. Cole, R. Dave, C. S. Frenk, N. Katz, and C. G. Lacey, *Astrophys. J.* **633**, 791 (2005)
 - [45] J. K. Parejko, T. Sunayama, N. Padmanabhan, D. A. Wake, A. A. Berlind, D. Bizyaev, M. Blanton, A. S. Bolton, F. van den Bosch, J. Brinkmann, et al., *Mon. Not. Roy. Astron. Soc.* **429**, 98 (2013)
 - [46] T. Nishimichi and A. Oka, *Mon. Not. Roy. Astron. Soc.* **444**, 1400 (2014)
 - [47] T. Okumura, M. Takada, S. More, and S. Masaki, *Mon. Not. Roy. Astron. Soc.* **469**, 459 (2017)
 - [48] Y. P. Jing and Y. Suto, *Astrophys. J.* **574**, 538 (2002)
 - [49] M. D. Schneider, C. S. Frenk, and S. Cole, *J. Cosmol. Astropart. Phys.* **5**, 030 (2012)
 - [50] C. Li, Y. P. Jing, A. Faltenbacher, and J. Wang, *Astrophys. J. Lett.* **770**, L12 (2013)
 - [51] Q. Xia, X. Kang, P. Wang, Y. Luo, X. Yang, Y. Jing, H. Wang, and H. Mo, *Astrophys. J.* **848**, 22 (2017)
 - [52] T. Okumura, U. Seljak, and V. Desjacques, *J. Cosmol. Astropart. Phys.* **11**, 014 (2012)
 - [53] M. D. Schneider and S. Bridle, *Mon. Not. Roy. Astron. Soc.* **402**, 2127 (2010)
 - [54] J. F. Navarro, C. S. Frenk, and S. D. M. White, *Astrophys. J.* **462**, 563 (1996)
 - [55] T. Okumura, N. Hand, U. Seljak, Z. Vlah, and V. Desjacques, *Phys. Rev. D* **92**, 103516 (2015)
 - [56] C. E. Rasmussen and C. K. I. Williams, *Gaussian Processes for Machine Learning* (2006).
 - [57] S. Ambikasaran, D. Foreman-Mackey, L. Greengard, D. W. Hogg, and M. O’Neil, *IEEE Transactions on Pattern Analysis and Machine Intelligence* **38** (2015)
 - [58] A. Lapi and A. Cavaliere, *Astrophys. J.* **692**, 174 (2009)
 - [59] A. Faltenbacher and S. D. M. White, *Astrophys. J.* **708**, 469 (2010)
 - [60] D. N. Spergel and P. J. Steinhardt, *Physical Review Letters* **84**, 3760 (2000)
 - [61] T. Okumura, et al., in preparation (2018).
 - [62] T. Okumura, T. Nishimichi, K. Umetsu, and K. Osato, *ArXiv e-prints* (2017), 1706.08860.
 - [63] To convert this to the one related to the observable quantity, one needs to replace the $(\mathbf{v}_g \cdot \mathbf{v}_c)$ term by $(v_g^z v_c^z)$, where $v_A^z(\mathbf{r})$ is the radial component of the peculiar velocity of sample A , $v_A^z(\mathbf{r}) = \mathbf{v}_A(\mathbf{r}) \cdot \hat{\mathbf{r}}$. Then the result will simply differ by a factor of 3.
 - [64] While we comprehensively analyze these statistics in Ref. [61], some results have been presented in the early version of this paper. See Ref. [62].